Calibration of an IMU Using 3-D Rotation Platform

3 authors, including:

Fabian Höflinger
University of Freiburg
41 PUBLICATIONS   **311** CITATIONS

Some of the authors of this publication are also working on these related projects:

Project   Unterwasser-Lokalisierung von Tauchenden (ULTa) View project

Calibration of an IMU Using 3-D Rotation Platform

Rui Zhang, Fabian Höflinger, and Leonhard M. Reindl, *Senior Member, IEEE*

Abstract—This paper presents complete procedures to calibrate an inertial measurement unit (IMU) using a 3-D rotation platform. Previous works show that all the sensors can be calibrated separately using different calibration tools or methods. However, there is no guarantee that all the calibrated sensors are aligned to one coordinate system. In consequence, existence of axes correlations between the sensors can have big impact on orientation or position determination. Besides, very few literatures report the detail of gyroscope calibration without professional facilities. Different from the previous works, the calibration procedures reported in this paper not only focus on the scalar and bias removal, but also cover the correction of angle correlations between different sensors. In addition, the calibration of gyroscope relying only on 3-D rotation platform is also given. The calibration results have been validated using professional calibration tools and commercial IMU module. As a result, our calibration approaches are able to achieve a similar calibration performance as the one using professional tools as well as minimize the angle correlations between sensors.

Index Terms—Calibration, inertial measurement unit (IMU), optimization, misalignment, correlation, scalar, bias.

I. INTRODUCTION

ONE OF THE key challenges in building Inertial Measurement Unit (IMU) module is that, the raw sensed data from the sensor is usually coupled with large bias, non-unitary scaling and misalignment error between three axes. Without a proper removal or compensation of these sensor errors - a process known as the calibration of sensor, the sensed data from IMU module can hardly be further processed to yield a consistent orientation or position estimations.

Since the calibration process is indispensable when using low-cost MEMS sensors, many works focusing on the field of sensor calibration have been published. Cheuk *et al.* presented a automatic calibration procedures for IMU module [1]. By rotating the sensors around all the axes by hand and keeping the sensors still at twelve different positions, the optimization problems of three cost functions i.e. the scaling factor, bias and misaligned angles for each sensor can be obtained. However, it is very difficult to determine angle misalignment matrix for compensating the angle correlation matrices of accelerometer

The authors are with the Department of Microsystems Engineering, University of Freiburg, Freiburg 79110, Germany (e-mail: rui.zhang@ imtek.uni-freiburg.de; fabian.hoeflinger@imtek.uni-freiburg.de; leonhard. reindl@imtek.uni-freiburg.de).

and magnetometer by simply minimizing the cost function, since the optimization process stops as long as the correct scaling and bias vectors are obtained. The gyroscope is calibrated using the information from other calibrated sensors but no detail information is given, similar as reported in [2]. However, the proposed gyroscope calibration is almost impossible to be carried out due to the nonlinear relation between the orientation update and angular rate as well as the noise introduced by other sensors.

Frosio *et al.* presented an accelerometer automatic procedure using Gauss-newton method and tested the calibrated accelerometer by comparing attitude angles (roll, pitch) with optical reference [3]. Similarly, this method also suffers from undetermined misalignment matrix. Merayo *et al.* provided an idea using 3D ellipsoid fitting to remove scalar, non-orthogonal and bias errors of a magnetometer [4]. However, how to remove the axes correlations was not mentioned in their work. Glueck *et al.* have developed a approach to calibrate the accelerometer automatically using (Unscented Kalman Filter) UKF and differentiating non-static and static status. The problem of this method is that UKF needs very long time to converge or become stable if either scaling, bias or misalignment error is large [5]. Following our previous work [6], this paper focuses on the complete calibration of all the sensors integrated in IMU module using least calibration tools. The aim of this study is to align all the sensors to the same coordinate system and calibrate gyroscope without additional assistance.

The remainder of this paper is structured as follows. In section II the sensor error model is presented. In section III the mathematic calibration approaches for all the sensors are given. The experimental result and numerical study are reported in section IV. Discussion and conclusion are given in section V.

II. MODELING OF SENSOR ERROR

The sensor bias vector for three axes is modeled as

$$\mathbf{o}_{sen} = [o_{x,sen}, o_{y,sen}, o_{z,sen}]^T, \tag{1}$$

where sen refers to sensor type, e.g. acc for accelerometer, gyr for gyroscope and mag for magnetometer.

The non-unitary scaling matrix is modeled as

$$\mathbf{S}_{sen} = \begin{bmatrix} ss_{x,sen} & 0 & 0 \\ 0 & ss_{y,sen} & 0 \\ 0 & 0 & ss_{z,sen} \end{bmatrix}. \tag{2}$$

The misalignment error matrix is modeled as

$$\mathbf{T}_{sen} = \begin{bmatrix} 1 & -\alpha_{yz,sen} & \alpha_{zy,sen} \\ \alpha_{xz,sen} & 1 & -\alpha_{zx,sen} \\ -\alpha_{xy,sen} & \alpha_{yx,sen} & 1 \end{bmatrix}, \tag{3}$$
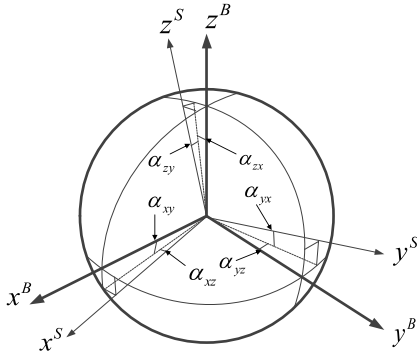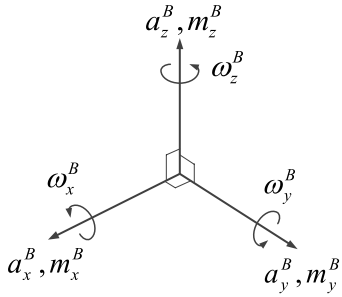
Fig. 1. Misalignment between axes [1].

Fig. 2. Axes of sensors alignment [1].

where $\alpha_{ij,sen}$ represents the small angle deviation of the ith sensitivity axis around the jth sensitivity axis of tri-axis sensor integrated in IMU module, as shown in Figs. 1 and 2 [1].

$\mathbf{a}^B = [a_x^B, a_y^B, a_z^B]^T$ is the acceleration vector in sensor body coordinate B measured by tri-axis accelerometer. $\boldsymbol{\omega}^B = [\omega_x^B, \omega_y^B, \omega_z^B]^T$ is the angular rate vector in sensor body coordinate B measured by tri-axis gyroscope. $\mathbf{m}^B = [m_x^B, m_y^B, m_z^B]^T$ is the magnetic field vector in sensor body coordinate B measured by tri-axis magnetometer. The misalignment error matrix can be factored into one rotation matrix for coordinate transformation of small-angle and one non-orthogonal misalignment matrix [7], as given by

$$\mathbf{T}_{sen} = \mathbf{T}_{R,sen}\mathbf{T}_{N,sen}. \tag{4}$$

$$\mathbf{T}_{R,sen} = \begin{bmatrix} 1 & -\alpha_{z,sen} & \alpha_{y,sen} \\ \alpha_{z,sen} & 1 & -\alpha_{x,sen} \\ -\alpha_{y,sen} & \alpha_{x,sen} & 1 \end{bmatrix}. \tag{5}$$

$$\mathbf{T}_{N,sen} = \begin{bmatrix} 1 & \xi_{z,sen} & -\xi_{y,sen} \\ 0 & 1 & \xi_{x,sen} \\ 0 & 0 & 1 \end{bmatrix}. \tag{6}$$

$\boldsymbol{\xi}_{sen} = [\xi_{x,sen}, \xi_{y,sen}, \xi_{z,sen}]^T$ is the non-orthogonal misalignment angle vector and $\alpha_{x,sen}, \alpha_{y,sen}, \alpha_{z,sen}$ represent the angle differences between coordinates of sensor S and IMU module B. The derivation detail of misalignment error matrix can be found in [8]. It is very important to note that $\mathbf{T}_{R,sen}$ is actually the approximation of multiplications of three misalignment matrices for each two axes when all the misalignment angles

are smaller, as given by

$$\mathbf{T}_{R,sen} \approx \mathbf{T}_{R,z,sen} \cdot \mathbf{T}_{R,y,sen} \cdot \mathbf{T}_{R,x,sen}. \tag{7}$$

$$\mathbf{T}_{R,z,sen} = \begin{bmatrix} \cos\alpha_{z,sen} & -\sin\alpha_{z,sen} & 0 \\ \sin\alpha_{z,sen} & \cos\alpha_{z,sen} & 0 \\ 0 & 0 & 1 \end{bmatrix}$$

$$\approx \begin{bmatrix} 1 & -\alpha_{z,sen} & 0 \\ \alpha_{z,sen} & 1 & 0 \\ 0 & 0 & 1 \end{bmatrix}. \tag{8}$$

$$\mathbf{T}_{R,y,sen} = \begin{bmatrix} \cos\alpha_{y,sen} & 0 & \sin\alpha_{y,sen} \\ 0 & 1 & 0 \\ -\sin\alpha_{y,sen} & 0 & \cos\alpha_{y,sen} \end{bmatrix}$$

$$\approx \begin{bmatrix} 1 & 0 & \alpha_{y,sen} \\ 0 & 1 & 0 \\ -\alpha_{y,sen} & 0 & 1 \end{bmatrix}. \tag{9}$$

$$\mathbf{T}_{R,x,sen} = \begin{bmatrix} 1 & 0 & 0 \\ 0 & \cos\alpha_{x,sen} & -\sin\alpha_{x,sen} \\ 0 & \sin\alpha_{x,sen} & \cos\alpha_{x,sen} \end{bmatrix}$$

$$\approx \begin{bmatrix} 1 & 0 & 0 \\ 0 & 1 & -\alpha_{x,sen} \\ 0 & \alpha_{x,sen} & 1 \end{bmatrix}. \tag{10}$$

If the misalignment angles are not small enough, sin and cos representation must be used. The notation *sen* refers to the sensor name, which is *acc*, *gyr* and *mag*.

III. SENSOR CALIBRATION APPROACHES

A. Theoretical Approach of Inertial Sensor Calibration

The inertial sensors used in this study are accelerometer and gyroscope, which measure the acceleration and the angular rate. The accelerometer error model is given as

$$\hat{\mathbf{a}}^B = \mathbf{S}_{acc}\mathbf{T}_{acc}(\tilde{\mathbf{a}}^S - \mathbf{o}_{acc}), \tag{11}$$

where $\hat{\mathbf{a}}^B = [\hat{a}_x^B, \hat{a}_y^B, \hat{a}_z^B]^T$ is the calibrated acceleration vector in IMU module coordinate B and $\tilde{\mathbf{a}}^S = [\tilde{a}_x^S, \tilde{a}_y^S, \tilde{a}_z^S]^T$ is the raw acceleration vector in sensor coordinate S read from accelerometer.

The calibration for the accelerometer aims to find the best fitted parameters in $\mathbf{S}_{acc}$, $\mathbf{T}_{acc}$ and $\mathbf{o}_{acc}$, which provide least error in the acceleration measurement. The number of parameters being solved is 12 in total including 9 elements from $\mathbf{S}_{acc}\mathbf{T}_{acc}$ and three elements in $\mathbf{o}_{acc}$. If N sets of measurements $\mathbf{y}_{acc}$ are available, 12 parameters are optimized by the following cost function

$$(\mathbf{S}_{acc}, \mathbf{T}_{acc}, \mathbf{o}_{acc}) = \underset{\mathbf{S}_{acc}, \mathbf{T}_{acc}, \mathbf{o}_{acc}}{\operatorname{argmin}} \sum_{n=1}^{N}(\left\|\mathbf{y}_{acc} - \hat{\mathbf{a}}^B\right\|)^2. \tag{12}$$

The same sensor error model as shown in (11) can also apply to gyroscope

$$\hat{\boldsymbol{\omega}}^B = \mathbf{S}_{gyr}\mathbf{T}_{gyr}(\tilde{\boldsymbol{\omega}}^S - \mathbf{o}_{gyr}), \tag{13}$$

where $\hat{\boldsymbol{\omega}}^B = [\hat{\omega}_x^B, \hat{\omega}_y^B, \hat{\omega}_z^B]^T$ is the calibrated angular rate vector in IMU module coordinate B and $\tilde{\boldsymbol{\omega}}^S = [\tilde{\omega}_x^S, \tilde{\omega}_y^S, \tilde{\omega}_z^S]^T$ is the raw angular rate vector in sensor coordinate S read from gyroscope.

Similarly, the cost function to optimize the parameters for gyroscope calibration is given by

$$(\mathbf{S}_{gyr}, \mathbf{T}_{gyr}, \mathbf{o}_{gyr}) = \underset{\mathbf{S}_{gyr}, \mathbf{T}_{gyr}, \mathbf{o}_{gyr}}{\mathrm{argmin}} \sum_{n=1}^{N} (\left\| \mathbf{y}_{gyr} - \hat{\boldsymbol{\omega}}^B \right\|)^2. \quad (14)$$

The Levenberg-Marquardt (LM) algorithm, which takes the advantages of gradient descent and the Gauss-Newton methods, is used to solve the optimization problems in (12) and (14). The detail derivation and algorithm procedures can be found in [9].

B. Theoretical Approach of Magnetometer Calibration

The magnetometer measures not only the constant earth magnetic field, but also the coupled magnetic noise induced from the nearby electronics, mechanical devices and ferromagnetic material. The same error model for accelerometer and gyroscope can be applied.

$$\hat{\mathbf{m}}^B = \mathbf{S}_{mag} \mathbf{T}_{mag} (\tilde{\mathbf{m}}^S - \mathbf{o}_{mag}), \quad (15)$$

where $\hat{\mathbf{m}}^B = [\hat{m}_x^B, \hat{m}_y^B, \hat{m}_z^B]^T$ is the calibrated magnetic field vector in IMU module coordinate B and $\tilde{\mathbf{m}}^S = [\tilde{m}_x^S, \tilde{m}_y^S, \tilde{m}_z^S]^T$ is the magnetic field vector in sensor coordinate S measured from magnetometer.

However, due to the soft-iron bias and hard-iron effect induced by the permanent magnets inherent and interaction of an external magnetic field with the ferromagnetic materials inside IMU module [10], large scaling, bias and misalignment error exist. Thus, LM algorithm requires careful tuning and longer time for convergence. In order to reduce the computational consumption, a two-step calibration method is applied. Rewrite (15) as

$$\hat{\mathbf{m}}^B = \mathbf{T}_{R,mag} \mathbf{S}'_{mag} (\tilde{\mathbf{m}}^S - \mathbf{o}_{mag})$$
$$= \mathbf{T}_{R,mag} \hat{\mathbf{m}}'^B, \quad (16)$$

where $\mathbf{S}'_{mag} = \mathbf{T}_{N,mag} \mathbf{S}_{mag}$.

The calibration schemes use the fact that the magnitude of magnetic flux vector is constant at any orientations, which means the normalized magnitude of magnetic field vector from the IMU module in local magnetic disturbance-free environment should always equal to 1. The first step calibration is equivalent to transforming a center-shifted and rotationally scaled ellipse to a circle. The aim is to find the best 3D ellipsoid that fits the measurement data set. The cost function for the first step is given by

$$(\mathbf{S}'_{mag}, \mathbf{o}_{mag}) = \underset{\mathbf{S}'_{mag}, \mathbf{o}_{mag}}{\mathrm{argmin}} \sum_{n=1}^{N} (1 - \left\| \hat{\mathbf{m}}'^B \right\|)^2. \quad (17)$$

$\mathbf{S}'_{mag}$ and $\mathbf{o}_{mag}$ describes the shape and the center of the ellipsoid. The ellipsoid equation is given as

$$(\tilde{\mathbf{m}}^S - \mathbf{o}_{mag})^T (\mathbf{S}'_{mag})^T \mathbf{S}'_{mag} (\tilde{\mathbf{m}}^S - \mathbf{o}_{mag})$$
$$= \left\| \mathbf{S}'_{mag} (\tilde{\mathbf{m}}^S - \mathbf{o}_{mag}) \right\| = 1. \quad (18)$$

Equation (18) can be expressed as a linear combination of $\tilde{\mathbf{m}}^S$ as $\|\mathbf{D} \cdot \mathbf{d}\| = 0$. $\mathbf{D}$ and $\mathbf{d}$ are given as

$$\mathbf{D} = [(\tilde{m}_x^S)^2, \tilde{m}_x^S, (\tilde{m}_y^S)^2, \tilde{m}_y^S, (\tilde{m}_z^S)^2, \tilde{m}_z^S,$$
$$\tilde{m}_x^S \tilde{m}_y^S, \tilde{m}_y^S \tilde{m}_z^S, \tilde{m}_x^S \tilde{m}_z^S, \mathbf{I}_{N \times 1}], \quad (19)$$

$$\mathbf{d} = [d_1, d_2, d_3, d_4, d_5, d_6, d_7, d_8, d_9, d_{10}]^T$$

$$= \begin{bmatrix} ss_x^2 \\ -2(ss_x^2 o_x + ss_x \xi_z o_y - ss_x \xi_y o_z) \\ \xi_z^2 + ss_y^2 \\ -2(ss_x \xi_z o_x + (\xi_z^2 + ss_y^2) o_y \\ + (-\xi_z \xi_y + ss_y \xi_x) o_z) \\ \xi_y^2 + xi_x^2 + ss_z^2 \\ -2(-ss_x \xi_y o_x + (-\xi_z \xi_y + ss_y \xi_x) o_y \\ + (\xi_y^2 + xi_x^2 + ss_z^2) o_z) \\ 2ss_x \xi_z \\ -2(\xi_z \xi_y - ss_y \xi_x) \\ -2ss_x \xi_y \\ \left\| \mathbf{S}' \mathbf{T}_R \mathbf{o} \right\| - 1 \end{bmatrix}, \quad (20)$$

where $\mathbf{I}_{N \times 1}$ stands for $N \times 1$ identity matrix. For simplicity in the notations, the footnote *mag* is ignored in (20).

If the vector $\mathbf{d}$ is known, it is possible to compute the elements of the matrix $\mathbf{S}'_{mag}, \mathbf{T}_{R,mag}$ and the components of the vector $\mathbf{o}_{mag}$. It can easily be done by algebraic manipulation of the expressions in the proper order. The following formulas show the relations between them and their expressions as functions of the components of $\mathbf{d}$ [4]:

$$ss_{x,mag} = \sqrt{d_1}$$
$$\xi_{z,mag} = \frac{d_7}{2\sqrt{d_1}}$$
$$\xi_{y,mag} = -\frac{d_9}{2\sqrt{d_1}}$$
$$ss_{y,mag} = \sqrt{d_3 - \frac{d_7^2}{4d_1}}$$
$$\xi_{x,mag} = \frac{2d_1 d_8 - d_7 d_9}{2\sqrt{4d_1^2 d_3 - d_1 d_7^2}}$$
$$ss_{z,mag} = \sqrt{d_5 - \frac{d_9^2}{4d_1} + (\frac{2d_1 d_8 - d_7 d_9}{2\sqrt{4d_1^2 d_3 - d_1 d_7^2}})^2} \quad (21)$$

$$\mathbf{o}_{mag} = \begin{bmatrix} -2d_1 & -d_7 & -d_9 \\ -d_7 & -2d_3 & -d_8 \\ -d_9 & -d_8 & -2d_5 \end{bmatrix}^{-1} \begin{bmatrix} d_2 \\ d_4 \\ d_6 \end{bmatrix}. \quad (22)$$

Now the cost function turns into

$$\mathbf{d} = \underset{\mathbf{d}}{\mathrm{argmin}} \|\mathbf{Dd}\|^2. \quad (23)$$

Singular Value Decomposition (SVD) can be used as a simple linear optimization approach to avoid iteration calculation. Under the condition of $\|\mathbf{d}\|^2 = 1$, $\mathbf{d}$ can be calculated as follows: firstly, calculate the SVD of $\mathbf{D}$

$$\mathbf{D} = \mathbf{D}_U \mathbf{D}_S \mathbf{D}_V^T, \quad (24)$$

where $\mathbf{D}_U$ is a $N \times N$ orthogonal matrix, $\mathbf{D}_S$ is a $N \times 10$ matrix with non-negative diagonal entries, and $\mathbf{D}_V$ is a 10×10

orthogonal matrix. The diagonal values of $\mathbf{D}_S$ are called singular value of $\mathbf{D}$, the column vectors of $\mathbf{D}_U$ are the left singular vectors of $\mathbf{D}$ and the column vectors of $\mathbf{D}_V$ are the right singular vectors of $\mathbf{D}$. Then the 10th column of $\mathbf{D}_V$ is the solution of $\mathbf{d}$. Detail information of optimization using SVD can be found in [11].

The second step calibration is to determine the small-angle rotation matrix $\mathbf{T}_{R,mag}$ by analyzing $\mathbf{m}'^B$. Detail of this calibration will be given in next section. Since the magnetometer has been rotated around three axes, the calibration procedure is divided into three phases, noted as phase-x, phase-y and phase-z. In each phase the sensor readings from two axis keep changing as sine wave and the other axis should remain unchanged. Since the rotation must cover 3D surface, at least one set of maximum and minimum points for each rotating axis can be found. E.g. define $k_{max,y/x}$ and $k_{min,y/x}$ as the maximum and minimum points of magnetic field vector in y-axis when the magnetic field vector in x-axis remains invariant. For the phase-x, the following conditions must be fulfilled:

$$\vec{\mathbf{T}}^{(1)}_{R,mag} \cdot \mathbf{m}'^B_{k_{\max(y/x)}} = \vec{\mathbf{T}}^{(1)}_{R,mag} \cdot \mathbf{m}'^B_{k_{\min(y/x)}} \quad (25)$$

$$\vec{\mathbf{T}}^{(1)}_{R,mag} \cdot \mathbf{m}'^B_{k_{\max(z/x)}} = \vec{\mathbf{T}}^{(1)}_{R,mag} \cdot \mathbf{m}'^B_{k_{\min(z/x)}} \quad (26)$$

$$\vec{\mathbf{T}}^{(1)}_{R,mag} \cdot \mathbf{m}'^B_{k_{\max(y/x)}} = \vec{\mathbf{T}}^{(1)}_{R,mag} \cdot \mathbf{m}'^B_{k_{\min(z/x)}} \quad (27)$$

$\vec{\mathbf{T}}^{(i)}_{R,mag}$ is the ith row in $\mathbf{T}_{R,mag}$, which contains three unknowns $\alpha_{x,mag}$, $\alpha_{y,mag}$ and $\alpha_{z,mag}$. $\mathbf{m}'^B_k = [m'^B_{x,k}, m'^B_{y,k}, m'^B_{z,k}]^T$.

The similar conditions apply to phase-y and phase-z. Therefore, 9 equations are used by optimization algorithm to compute $\alpha_{x,mag}$, $\alpha_{y,mag}$ and $\alpha_{z,mag}$, so as to determine the small-angle misalignment matrix $\mathbf{T}_{R,mag}$.

The theoretical approaches are actually very difficult to apply practically. Since all the calibration procedures are implemented using different calibration tools, the resulted calibrated sensor data are along the coordinates of different calibration tools respectively. Therefore, it does not guarantee that all the axes from three different sensors are in the same coordinate system, neither the correct misalignment matrices of the IMU module of three sensors can be obtained. The calibration performance of theoretical approach really depends on how accurate the IMU module is placed or attached on different calibration tools and how well the sensor IC chips are soldered on the PCB.

In order to overcome this issue, the data read from accelerometer and gyroscope during the calibration of magnetometer are utilized to compensate the misalignment angles between accelerometer/gyroscope and magnetometer using the similar approaches from the second step of magnetometer calibration.

Since the small-angle coordinate transformation matrix needs to be recalculated at this stage, the cost function for accelerometer given in (12) is also divided into two steps in a similar manner as magnetometer calibration procedures. The first step is to find out $\mathbf{o}_{acc}$, $\mathbf{S}_{acc}$ and $\mathbf{T}_{N,acc}$. Afterwards, the exact same equation as (25)-(27) can be applied to determine $\mathbf{T}_{R,acc}$, since the change of gravity vector is similar to the change of magnetic field flux. However, instead of showing

only the low frequency component by magnetometer, the accelerometer is more sensitive to any kind of movement during the 3D rotation. Therefore, a low pass filter needs to be applied firstly to remove high frequency component in order to easily find the maximum and minimum points. It also leads to faster computation for determining the small-angle difference by applying the filtered data to the optimization algorithm.

The calibration procedures for determining the small-angle coordinate transformation matrix of gyroscope are different. When rotating around one axis, only the sensor data reading from this axis shows non-zero angular rate values and the sensor data readings from other two axes remain zero. Similarly the calibration procedures are divided into three phases, namely phase-x, phase-y and phase-z. However the phases are named after the rotating axis instead of non-rotating axes. Since no more maximum and minimum points can be found, two points at 1/3 and 2/3 time duration within one phase are chosen. During phase-x the corresponded time step is notated as $k_{x,1}$ and $k_{x,2}$, and the following conditions must be fulfilled:

$$\vec{\mathbf{T}}^{(2)}_{R,gyr} \cdot \boldsymbol{\omega}'^B_{k_{x,1}} = 0 \quad (28)$$

$$\vec{\mathbf{T}}^{(2)}_{R,gyr} \cdot \boldsymbol{\omega}'^B_{k_{x,2}} = 0 \quad (29)$$

$$\vec{\mathbf{T}}^{(3)}_{R,gyr} \cdot \boldsymbol{\omega}'^B_{k_{x,1}} = 0 \quad (30)$$

$$\vec{\mathbf{T}}^{(3)}_{R,gyr} \cdot \boldsymbol{\omega}'^B_{k_{x,2}} = 0 \quad (31)$$

Similar conditions must fulfill in other two phases. Notice that a low pass filter has been applied before the optimization algorithm to achieve fast convergence. Similarly the calibration of gyroscope has also been divided into two steps. $\boldsymbol{\omega}'^B = [\omega'^B_x, \omega'^B_y, \omega'^B_z]^T$ is the calibration result after first step calibration.

IV. EXPERIMENTS AND NUMERICAL STUDY

Three sensors are calibrated separately using different experimental setups and approaches. Since the attachment of the IMU module to the calibration tools are manually done, the misalignment angles for different calibration experiment are not the same. Therefore, the calibration of inertial sensors are also divided into two steps as magnetometer. In such way, the misalignment angles of three sensors can be calibrated by mapping all the sensors to the same coordinate.

A. Magnetometer Calibration

In order to find the best 3D ellipsoid that fits the measurement data set so as to accomplish the first step calibration, the measurement data set must be able to describe the 3D space as completely as possible, i.e. the magnetometer should fully rotate (360°) about all the axes. The experiment was carried out in the outdoor environment by using a self-build plastic 3D rotation machine shown in Fig. 3, so that the magnetometer has a sufficient distance from ferromagnetic objects and the sensed local magnetic field is not disturbed. The uncalibrated magnetic field flux is shown in Fig. 4.

It can be seen that there are some scalar and misalignment errors resulting in a variant normalized value affected by
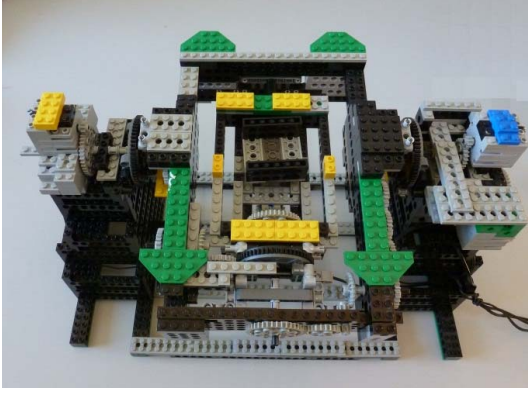
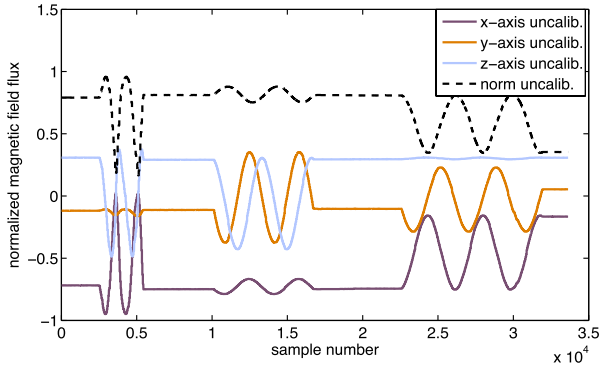Fig. 3.   Self-build plastic 3D rotation machine.

Fig. 4.   Magnetic field vector and its magnitude before calibration.
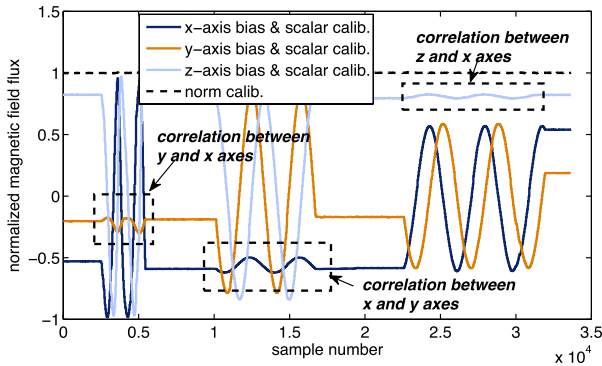

Fig. 5.   Magnetic field vector and its magnitude after first step calibration.
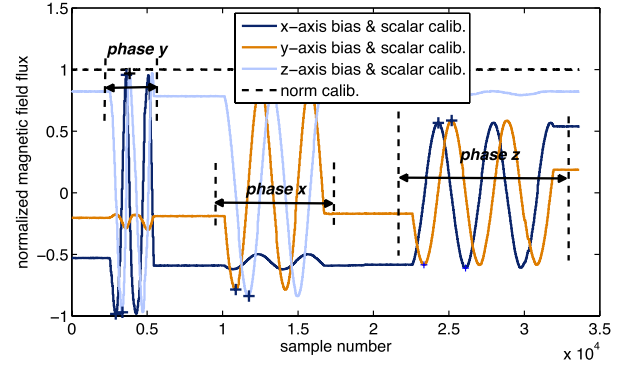

Fig. 6.   Three phases of magnetic field vector and its magnitude after first step calibration.
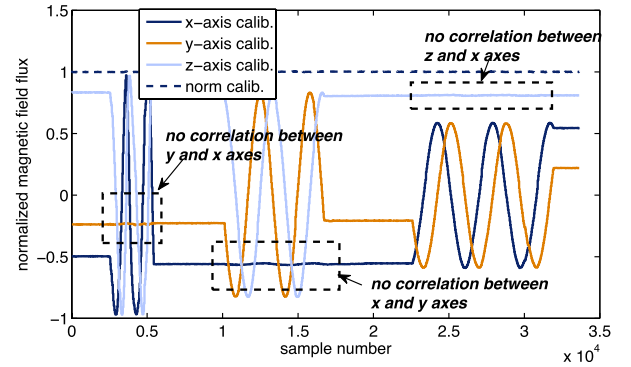

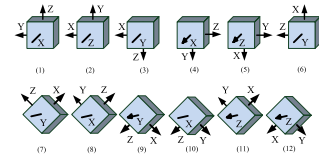Fig. 7.   Magnetic field vector and its magnitude after second step calibration.

Fig. 8.   Twelve positions of the IMU to calibrate the accelerometer.

rotations. After implementing a LM optimization algorithm based on the cost function (17), the scalars and non-orthogonal misalignment matrix are successfully calibrated as depicted in Fig. 5.

The second step calibration is to determine three small angles from the small-angle coordinate transformation matrix $\mathbf{T}_{R,mag}$ in (16) so that the correlations between axes highlighted inside the dash rectangular boxes given in Fig. 5 can be removed. Three phases where two axes are rotating and the other one keeps constant are defined, i.e. y-, x- and z-axis are supposed to be constant in phase y, x, and z respectively.

The black cross marks in each phase as shown in the Fig. 6 represent two sets of data corresponding to the maximum

and minimum magnetic field values for the two rotating axes. They are used to solve equations (25) (26) and (27) for each phase to eventually determine three small angles to compensate the small-angle coordinate transformation. After obtaining $\mathbf{T}_{R,mag}$, the correct magnetic field vector in coordinate B: $\hat{\mathbf{m}}^B$ is achieved and depicted in Fig. 7. As can be seen in the figure, one axis is able to remain invariant when other two axes are rotating.

B. Accelerometer Calibration

Since the accelerometer does not only measure the acceleration due to the movement but also the gravity, a static calibration procedure is carried out to avoid the affect of the movement [12]. The IMU module is mounted inside a hollow metal cube, where the sensor axes are aligned with the ones of the cube. As indicated in Fig. 8, the cube is placed in 12 different positions: six positions (1, 2, 3, 4, 5, 6) are orthogonal positions to the ground, the other six positions (7, 8, 9, 10, 11, 12) are in 45° to ground
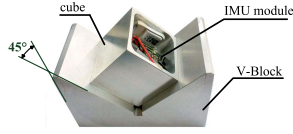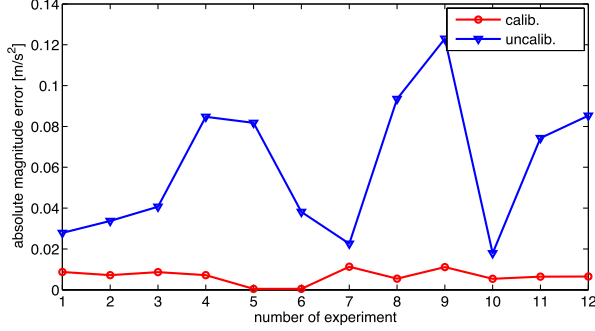
Fig. 9.   Hollow cube and V-block.

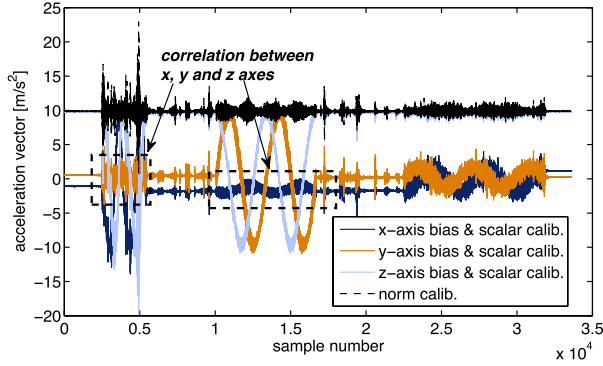Fig. 10.   Absolute magnitude error between calibrated and uncalibrated acceleration data.

Fig. 11.   Acceleration vector and its magnitude after first step calibration.

using the V-block depicted in Fig. 9. Accelerometer output is recorded to calculate the acceleration magnitude (norm value) $\|\mathbf{a}^B\| = \sqrt{(a_x^B)^2 + (a_y^B)^2 + (a_z^B)^2}$ of each position. Then the magnitude values are compared with the local gravity value $g \approx 9.81 \text{m/s}^2$, since in static condition, the $\|\mathbf{a}^B\|$ should equal to g.

Since accelerometer has to be calibrated in the similar manner as magnetometer, the accelerometer calibration cost function for the cube experiment is given as

$$(\mathbf{S}'_{acc}, \mathbf{o}_{acc}) = \underset{\mathbf{S}'_{acc}, \mathbf{o}_{acc}}{\operatorname{argmin}} \sum_{n=1}^{N} (g - \|\mathbf{a}'^B_n\|)^2, \qquad (32)$$

where $\mathbf{S}'_{acc} = \mathbf{T}_{N,acc}\mathbf{S}_{acc}$.

After determining $\mathbf{S}_{acc}$, $\mathbf{T}_{N,acc}$ and $\mathbf{o}_{acc}$, the absolute magnitude errors of 12 positions between calibrated/uncalibrated acceleration data sets and local gravity value are shown in Fig. 10.

The acceleration vector after scalar correction is shown in Fig. 11. It can be seen that the norm value of static acceleration equals to gravity g. However, small correlation between axes can still be found. Therefore the small-angle coordinate transformation matrix needs to be found.
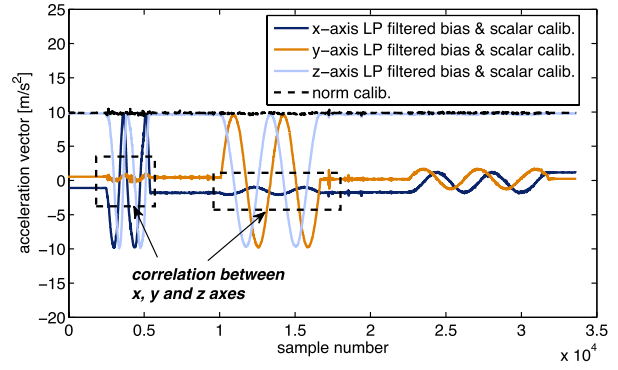

Fig. 12.   LP filtered acceleration vector and its magnitude after first step calibration.
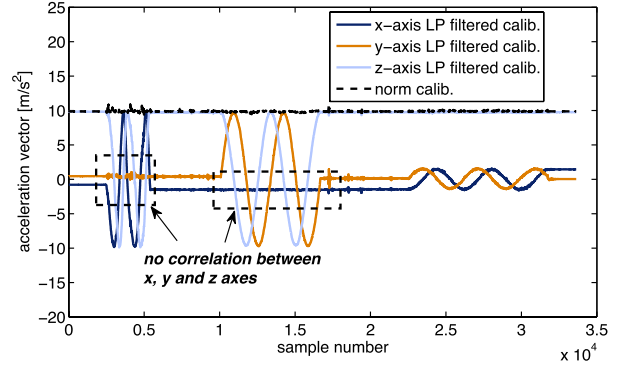

Fig. 13.   LP filtered acceleration vector and its magnitude after second step calibration.

The similar approaches reported in magnetometer calibration are applied to remove the correlation between axes, so as to map the acceleration coordinate to the coordinate of calibrated magnetometer. In order to find data points corresponding to the maximum and minimum accelerations, a low pass filter is firstly applied to suppress the high frequency component due to the movement. The low pass (LP) filtered acceleration vector is shown in Fig. 12.

After solving the equations (25) (26) and (27) for each phase, the calibration result after correction of small-angle coordinate transformation is given in Fig. 13.

It is worth to be mentioned that the calibration procedure of accelerometer can also be implemented without the hollow cube. In this way, the accelerometer must be held still in 12 position without any movement.

C. Gyroscope Calibration

Two calibration approaches for gyroscope will be given. The first one relies on a professional rotation table and the other one requires no additional calibration tools.

1) Gyroscope Calibration Using Calibration Tools: Similar as calibration of accelerometer, the gyroscope calibration cost function for the first step is given as

$$(\mathbf{S}'_{gyr}, \mathbf{o}_{gyr}) = \underset{\mathbf{S}'_{gyr}, \mathbf{o}_{gyr}}{\operatorname{argmin}} \sum_{n=1}^{N} (\|\boldsymbol{\omega}^B - \hat{\boldsymbol{\omega}}'^B\|)^2, \qquad (33)$$

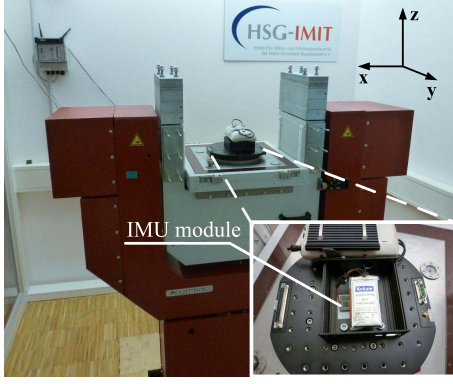where $\mathbf{S}'_{gyr} = \mathbf{T}_{N,gyr}\mathbf{S}_{gyr}$.
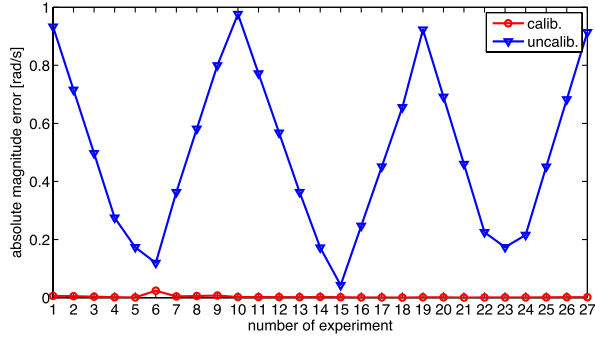
Fig. 14.   Rotation table.

Fig. 15.   Absolute magnitude error between calibrated and uncalibrated angular rate data.

In order to determine the 9 unknown parameters in $\mathbf{S}'_{gyr}$ and $\mathbf{o}_{gyr}$, the IMU module is mounted to a rotation table so that the IMU module is able to rotate with constant angular velocities, as shown in Fig. 14. In the experiment the IMU module was rotated with 9 different angular rates from $-400^{\circ}/s$ to $400^{\circ}/s$ with the change step of $100^{\circ}/s$ around x-, y- z-axis of coordinate B respectively.

After determining $\mathbf{S}'_{gyr}$ and $\mathbf{o}_{gyr}$, the absolute magnitude errors of gyroscope in 27 experiments between calibrated/uncalibrated angular rate data sets are depicted in Fig. 15.

The correction procedure of small-angle coordinate transformation matrix is similar to the ones from magnetometer and accelerometer calibrations. The calibration detail will be given in the next calibration approach.

2) Gyroscope Calibration Without Calibration Tools: According to the previous calibration procedures it is possible to determine $\mathbf{T}_{R,gyr}$ and $\mathbf{o}_{gyr}$ without calibration tools or machines if some conditions are fulfilled. For example, $\mathbf{o}_{gyr}$ could be derived by keeping the sensor still and talking the mean of the sensor data set, $\mathbf{T}_{R,gyr}$ could be determined using the same approach and the same data set from magnetometer calibration. However, the white sensor noise and no sine-like rotation curve add more uncertainties and difficulties to the calibration. Although the Allan variance can be used to obtain required time period for bias averaging, the sensor must be maintained still in the laboratory environment for significant period of time, which is not always possible for some users or applications.

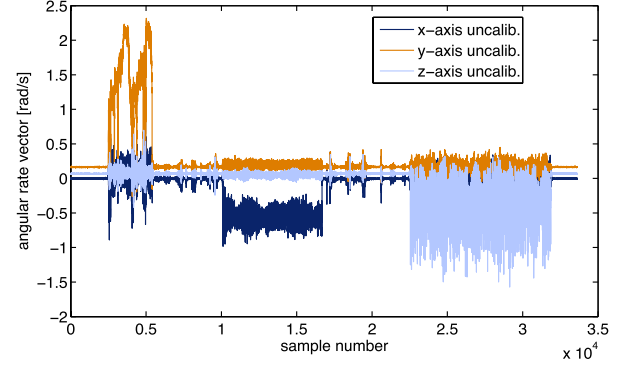|	$\hat{o}_{gyr,x}$	$\hat{o}_{gyr,y}$	$\hat{o}_{gyr,z}$
w. tools	0.0027	0.1605	0.0660
LS	-0.0022	0.1608	0.0679

Fig. 16.   The angular rate vector before bias removal.

In this paper the bias determination using least squares (LS) based line fitting is presented. At each time step, the gyroscope outputs of each axis from the start time step up to the current time step are summed up, which are set as the data of y-axis, and sample number is set as the data of x-axis. Therefore, the determination of bias equals to finding the slope of the fitted line.

$$y_{x,i} = \sum_{k=1}^{i} \omega_{x,k} \qquad (34)$$

The slope of x-axis using LS based line fitting is given by

$$\hat{o}_{gyr,x} = \frac{(\sum x_i y_{x,i}) - (\sum x_i)\bar{y}_x}{(\sum x_i^2) - (\sum x_i)\bar{x}}. \qquad (35)$$

x_i equals to i, $\sum x_i$ is the sum of x_i, $\sum x_i^2$ is the sum of the squares of x_i, $\sum x_i y_{x,i}$ is the sum of the products of corresponding x_i and $y_{x,i}$, $\bar{x}$ is the mean of x_i, and $\bar{y}_x$ is the mean of $y_{x,i}$. $\hat{o}_{gyr,y}$ and $\hat{o}_{gyr,y}$ are calculated in a similar way.

In comparison with taking the mean of gyroscope outputs directly, LS line fitting does not suffer from outliers. Averaging might deliver different bias result according to different choice of data set, such as the length of the data set. To the contrary, the LS approach is more robust against noise variation. Table I shows the obtained gyroscope bias using calibration tools and LS based approach.

The angular rate vectors before and after removing bias are shown in Figs. 16 and 17.

For small-angle coordinate transformation correction, the data set during 3D rotation experiment for magnetometer calibration is used to remove the correlation between axes. However, it is not easy to compensate the correlations between other axes since there are some rapid changes in all the axes and the correlations are not explicit. Therefore a low pass filter is applied similarly as accelerometer calibration to suppress high frequency component so that the correlations between axis can be extracted. The LP filtered unbiased angular rate
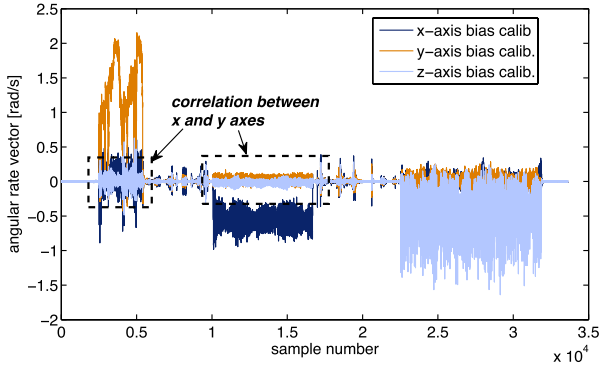
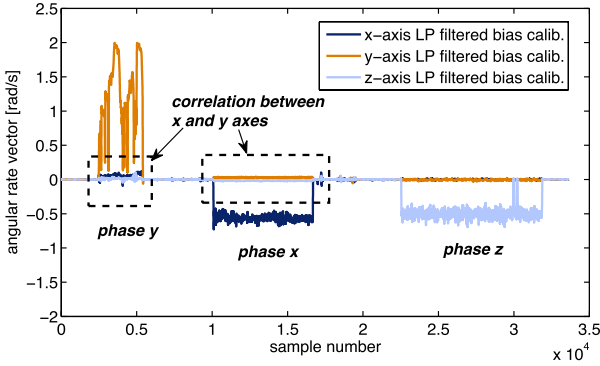Fig. 17. The angular rate vector after bias removal.

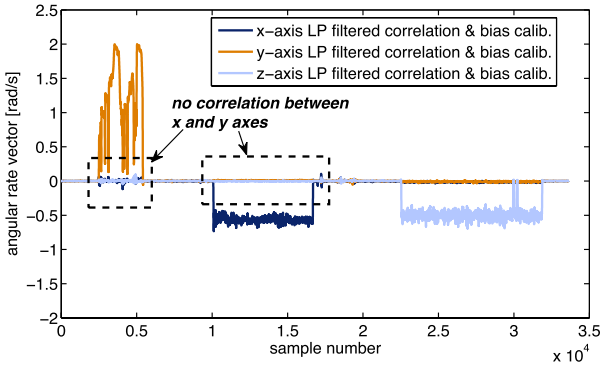Fig. 18. LP filtered unbias angular rate vector before misalignment angle correction.

Fig. 19. LP filtered unbias angular rate vector after misalignment angle correction.

vector is given in Fig. 18, from which it can be seen clearly that there is correlation between x- and y-axis.

After solving equations (28), (29), (30) and (31) for each phase, the small-angle coordinate transformation matrix $\mathbf{T}_{R,gyr}$ is achieved. The LP filtered unbiased and correlation-free angular rate vector is depicted in Fig. 19.

The last step of the calibration is to obtain the scalar of all the axes. After misalignment angle correction, only one axis is rotating at each time. Therefore, the scalar can be simply determined by comparing the orientation (angle) change of each axis based on accelerometer/magnetometer and the angle change by integrating angular rate of each axis over time [13],

TABLE II

COMPARISON OF GYROSCOPE SCALAR VALUE BETWEEN CALIBRATION WITH AND WITHOUT TOOLS

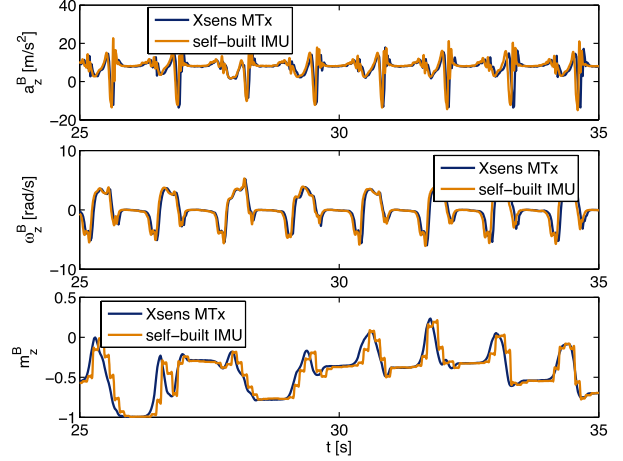|	$\hat{SS}_{gyr,x}$	$\hat{SS}_{gyr,y}$	$\hat{SS}_{gyr,z}$
w. tools	1.1526	1.1327	1.1425
w/o. tools	1.1526	1.1327	1.1411

Fig. 20. Comparison of calibrated sensor data and output of Xsens MTx.

as given by

$$\hat{SS}_{gyr,x} = \text{abs}\left(\frac{\theta'_{x,k_x+N_x} - \theta'_{x,k_x}}{\sum_{k=k_x}^{k_x+N_x} \omega'_{x,k} t_s}\right),$$
$$\hat{SS}_{gyr,y} = \text{abs}\left(\frac{\theta'_{y,k_y+N_y} - \theta'_{y,k_y}}{\sum_{k=k_y}^{k_y+N_y} \omega'_{y,k} t_s}\right),$$
$$\hat{SS}_{gyr,z} = \text{abs}\left(\frac{\theta'_{z,k_z+N_z} - \theta'_{z,k_z}}{\sum_{k=k_z}^{k_z+N_z} \omega'_{z,k} t_s}\right), \quad (36)$$

where k_x, k_y and k_z are the rotation start point for three axes, and N_x, N_y and N_z are the step lengths of three rotations. θ'_x, θ'_y and θ'_z stand for the roll, pitch and yaw angles of Euler angles obtained by accelerometer and magnetometer. The detail about orientation update can be found in [14]. abs($\cdot$) stands for taking the absolute value. Table II shows the obtained gyroscope scalars with and without calibration tools.

It is very important to note that the calibration order should not be changed and scalar calibration must be implemented after the correction of correlations. The reason is that the orientation update using Euler angle is not a linear process, and Euler angle change equaling to the direct integration of angular rate over time fulfills only when one axis is rotating and the other two axes remain still.

Since the Xsens IMU is calibrated using professional calibration tools in laboratory environment, the output of IMU module MTx from Xsens is used as a reference. The calibration performance is shown in Fig. 20. It can be seen that the magnitude of sensed data using proposed calibration procedures is almost identical to the one of MTx. However, time shifts between two data sets can be found, since data missing can occur during the RF transmission. Besides, the update

rate of the magnetometer (10 Hz) is too low in comparison with MTx. These issues will be improved in the future by using Bluetooth communication and a new magnetometer with a higher update rate.

V. CONCLUSION

Calibration procedures for accelerometer, gyroscope and magnetometer are given in this paper. For the calibration of magnetometer, the procedures are divided into two steps. The reason is that on one hand, 12 unknowns can not be completely determined by directly applying the LM algorithm to the cost function of magnetometer due to the lack of measurement i.e., $\left\|\mathbf{m}^B\right\| = 1$. On the other hand, large scaling and bias error caused by ferromagnetic components from the IMU module make the convergence of LM algorithm very difficult. The first step is to calibrate scaling, non-orthogonal matrices and vector bias. It can be clearly seen from Fig. 4 that after the first step calibration, the scaling, non-orthogonal and bias error are successfully removed, since the calibrated magnetic flux magnitude equals to 1. The second step is to transform the magnetic field vector from sensor coordinate S to IMU module coordinate B. Under the condition that one axis remains as a constant when other two axes are rotating, three small-angles in $\mathbf{T}_{R,mag}$ can be determined by solving the equations. As shown in Fig. 7, the highlight regions in Fig. 5 have been corrected.

The accelerometer is calibrated in a static manner, whose performance will not be degraded by accelerations due to the movement. With the experiments of 12 different positions, 12 unknowns in (11) can be determined. However, as the calibration experiments for each sensor are independent of each other, the obtained misaligned small angles of the previous experiment might not fit the next experiment. Thus, the static experiment is used to only obtain the 9 unknown given in (32). As shown in Fig. 10, the magnitude error of calibrated accelerometer is significantly reduced in comparison of the one of uncalibrated sensor. The angle correlations in coordinate B are then compensated using the data set from magnetometer calibration experiment, as shown in Fig. 13.

Two approaches for gyroscope calibration are reported. When no calibration tools is available, the bias of gyroscope is firstly determined by finding the slope of LS based fitted line. Then the small-angle coordinate transformation matrix is calibrated using the similar way as magnetometer calibration by solving the equations (28), (29), (30) and (31) for each phase. As can be seen from Fig. 19, the correlations between axes shown in Fig. 18 have been significantly compressed. At the end, the scalar is calculated by comparing the orientation change based on calibrated accelerometer/magnetometer and angle change computed from the integration of angular rate. When using rotation table, the scalar, bias and non-orthogonal misalignment matrix of gyroscope are calibrated using 27 data sets with different angular rates for different axes. As can be seen from Fig. 15, the magnitude error of calibrated gyroscope is significantly reduced in comparison of the one of uncalibrated sensor. Afterwards, the same procedures for compensating the small-angle coordinate transformation

matrix are applied so as to align the coordinate of gyroscope to the coordinate of IMU module. Tables I and II show that the obtained bias and scalar values from both approaches are very close. It is necessary to mention that the non-orthogonal misalignment matrix $\mathbf{T}_{N,gyr}$ can not be obtained due to insufficient reference data if no calibration tools are available. Fortunately, non-orthogonal misalignment normally has been corrected during sensor manufacture.

Since all the sensors are calibrated off-line, the future work is to find an on-line calibration approaches using iterative algorithm on the condition that the calibration accuracy is not decreased.

REFERENCES

[1] C. M. Cheuk, T. K. Lau, K. W. Lin, and Y. Liu, "Automatic calibration for inertial measurement unit," in *Proc. 12th ICARCV*, Dec. 2012, pp. 1341–1346.

[2] W. T. Fong, S. K. Ong, and A. Y. C. Nee, "Methods for in-field user calibration of an inertial measurement unit without external equipment," *J. Meas. Sci. Technol.*, vol. 19, no. 8, pp. 085202-1–085202-11, Jul. 2008.

[3] I. Frosio, F. Pedersini, and N. A. Borghese, "Autocalibration of MEMS accelerometers," *IEEE Trans. Instrum. Meas.*, vol. 58, no. 6, pp. 2034–2041, Jun. 2009.

[4] J. M. G. Merayo, P. Brauer, F. Primdahl, J. R. Petersen, and O. V. Nielsen, "Scalar calibration of vector magnetometers," *J. Meas. Sci. Technol.*, vol. 11, no. 2, pp. 120–132, Feb. 2000.

[5] M. Glueck, A. Buhmann, and Y. Manoli, "Autocalibration of MEMS accelerometers," in *Proc. IEEE I2MTC*, May 2012, pp. 1788–1793.

[6] F. Hoeflinger, R. Zhang, J. Mueller, W. Burgard, and L. M. Reindl, "A wireless micro inertial measurement unit (WIMU)," *IEEE Trans. Instrum. Meas.*, vol. 62, no. 8, pp. 2583–2595, Aug. 2013.

[7] M. E. Pittelkau, "Everything is relative in spacecraft system alignment calibration," *J. Spacecraft Rockets*, vol. 39, no. 3, pp. 460–466, Jun. 2002.

[8] L. Pfeifer, "Orthogonalization of nonorthogonal vector components [inertial navigation]," in *Proc. Navigat. 21st Century IEEE PLANS*, Nov. 1988, pp. 553–559.

[9] H. Gavin, "The Levenberg–Marquardt method for nonlinear least squares curve-fitting problems," Ph.D. dissertation, Dept. Civil Environ. Eng., Duke Univ., Durham, NC, USA, Sep. 2011.

[10] J. Vasconcelos, G. H. Elkaim, C. Silvestre, P. Oliveira, and B. Cardeira, "A geometric approach to strapdown magnetometer calibration in sensor frame," in *Proc. IFAC Workshop, NGCUV*, 2008, pp. 172–177.

[11] S. B. Himane and D. Zikic, "Singular value decomposition, basic mathematical tools for imaging and visualization," in *Lecture Note, Chair for Computer Aided Medical Procedures and Augmented Reality, and Control of Underwater Vehicles*. München, Germany: Technische Universitaet München, 2006.

[12] K. S. Tee, M. Awad, A. Dehghani, D. Moser, and S. Zahedi, "Triaxial accelerometer static calibration," in *Proc. WCE*, Jul. 2011, pp. 1–4.

[13] M. Looney, *A Simple Calibration For MEMS Gyroscopes*. Norwood, MA, USA: Analog Device, 2010.

[14] R. Zhang, F. Hoeflinger, and L. M. Reindl, "Inertial sensor based indoor localization and monitoring system for emergency responders," *IEEE Sensors J.*, vol. 13, no. 2, pp. 838–848, Feb. 2013.

Rui Zhang received the B.Sc. degree from the Beijing University of Aeronautics and Astronautics, Beijing, China, and the M.Sc. degree from the Institute of Telecommunications, Darmstadt University of Technology, Darmstadt, Germany, in 2006 and 2009, respectively. He is currently pursuing the Ph.D. degree in indoor localization technologies at the Laboratory for Electrical Instrumentation, Institute of Microsystem Technology, Albert-Ludwigs University of Freiburg, Germany. His current research interests include wireless infrastructure-based localization, inertial sensor-based localization, human movement monitoring, and classification. He was a recipient of the Siemens Master Program Scholarship for the Master study in Germany in 2006.

Fabian Höflinger received the B.Sc. degree in automation engineering from the University of Applied Sciences, Friedrichshafen, Germany, and the master's degree in automation and energy systems from the University of Applied Sciences, Mannheim, Germany, in 2007. He is currently pursuing the Ph.D. degree in indoor-localization systems at the Laboratory for Electrical Instrumentation, Institute of Microsystem Technology, Albert-Ludwigs University of Freiburg, Freiburg, Germany.

He was with Junghans Feinwerktechnik, Schramberg, Germany, where he developed components for telemetric systems. He developed inductive electronic components for programmable fuses. From 2007 to 2010, he was with a company of telemetric systems, where he was involved in inductive measurement and signal transformation.

Leonhard M. Reindl received the Diploma degree in physics from Technische Universität München, Munich, Germany, and the Dr. sc. techn. degree from the Vienna University of Technology, Vienna, Austria, in 1985 and 1997, respectively. He joined the Surface Acoustic Wave Department, Siemens Corporate Technology Division, Munich, in 1985, where he was involved in the development of surface acoustic wave (SAW) devices for signal processing and matched filtering in radio communications, radar systems, SAW-based identification marks, and wireless passive SAW-based sensors. In 1999, he joined the Institute of Electrical Information Technology, Clausthal University of Technology, Clausthal-Zellerfeld, Germany. In 2003, he was a Full Professor of electrical instrumentation with the Institute for Microsystem Technology, Albert-Ludwigs University of Freiburg, Freiburg, Germany. He has authored or co-authored more than 250 papers on SAW devices and wireless passive sensor systems and holds 45 patents. His current research interests include wireless sensor systems, energy-harvesting systems, local positioning systems, and search and rescue systems for people buried in disasters.

Dr. Reindl is a member of the Technical Program Committees of the IEEE Frequency Control Symposium, the IEEE Ultrasonic Symposium, Eurosensors, Sensors, and the German Biannual Symposium "Sensoren und Messsysteme." He was an Elected Member of the AdCom of the IEEE UFFC Society from 2005 to 2007 and from 2010 to 2012.